Renewable Energy 188 (2022) 269–281

Contents lists available at ScienceDirect

Renewable Energy

journal homepage: www.elsevier.com/locate/renene

Predictive capability of actuator disk models for wakes of different wind turbine designs

Guodan Dong [a, b, 1], Zhaobin Li [a, b, 1], Jianhua Qin [a, b], Xiaolei Yang [a, b, *]

[a] The State Key Laboratory of Nonlinear Mechanics, Institute of Mechanics, Chinese Academy of Sciences, Beijing, 100190, China
[b] School of Engineering Sciences, University of Chinese Academy of Sciences, Beijing, 100049, China

ARTICLE INFO

Article history:
Received 8 May 2021
Received in revised form
14 December 2021
Accepted 7 February 2022
Available online 12 February 2022

Keywords:
Actuator disk model
Actuator surface model
Wind turbines wakes
Different turbine designs

ABSTRACT

To evaluate the predictive capability of the actuator disk (AD) models in simulating wakes of different wind turbine designs, we compare the results of the AD simulation with those of the actuator surface (AS) simulation for the EOLOS, NREL and a variant of the NREL (i.e., NREL-V) wind turbine designs. Two types of AD models are considered, i.e., the AD-R and AD-NR models corresponding to the AD model with and without rotational effects, respectively. For the AD models, the force coefficients are both obtained from the corresponding AS simulations. The results from the AD simulation are compared with those of AS simulations. It is observed that the velocity profiles predicted by the AD models agree well with the AS predictions. For the turbulent kinetic energy and the Reynolds shear stress, differences appear at far wake locations (7*D*, and 9*D* downwind of the turbine where *D* is the rotor diameter) for both the EOLOS and the NREL-V turbines. In case of the NREL turbine, on the other hand, there is an overall good agreement except in 3*D* downwind to the turbine. Furthermore, the modes obtained by using the proper orthogonal decomposition from the AD and AS simulations are also presented and compared with each other, indicating that the distribution of the mode energy, and the location and features of the mode patterns differ for different turbine designs.

1. Introduction

The commitment of countries to become carbon neural in the next few decades calls for increasing research efforts to reduce the levelized cost of wind energy because of its renewability and sustainability. The wind energy comes from the kinetic energy in the large-scale motion of the air above the atmospheric boundary layer (ABL), which is driven by the solar energy and buoyancy. Wind turbines often clustered together to form wind farms [1,2]. In a wind farm, the wake of an upstream turbine influences its downwind neighbors with reduced oncoming velocity and increased velocity fluctuations, resulting in a loss of power output and an increase of fatigue loads [1,3]. Depending on the wind farm layout and wind conditions, the power loss of the downwind turbine ranges from 20% to 80% with a common 40% loss in full-wake conditions [4,5].

Continuous research effort has been made to understand the mechanism of the wake dynamics. Various tools have been employed to predict wind turbine wakes with different model fidelities. Among them, semi-analytical wake models [6–9] are capable of providing fast estimation of the wake. However, certain simplifications (such as linear wake expansion and predefined velocity profile) and calibrated parameters for standard scenarios are often included in these models. As an alternative approach, computational fluid dynamics (CFD) simulations which predict the wake evolution by solving the fundamental governing equations of fluid flow [10], are able of providing more detailed wake structures and are particularly suitable for non-standard scenarios, such as complex terrain topology [11–14] and yaw misalignment of the turbine [15,16]. Due to the multi-scale nature of the flow phenomenon involved, it is still difficult, if not impossible, to resolve all the small scale flow structures of several centimeters on the boundary layer of the blade boundary [12] in wind turbine and farm simulations. Instead, wind turbines are often parametrized with actuator type models to reduce the computational cost, including the actuator disk (AD) model, the actuator line (AL) model and the actuator surface (AS) model.

* Corresponding author. The State Key Laboratory of Nonlinear Mechanics, Institute of Mechanics, Chinese Academy of Sciences, Beijing, 100190, China.
E-mail address: xyang@imech.ac.cn (X. Yang).
[1] These two authors contributed equally.

https://doi.org/10.1016/j.renene.2022.02.034
0960-1481/

The AD model, which was developed by Rankine [17] and Froude [18] for propeller calculations, represents the turbine blade as a permeable disk interacting with wind. Because of its theoretical simplicity and computational efficiency, this model is widely used in wind turbine and wind farm simulations [19–21]. In most AD models, the uniformly distributed thrust forces applied on the disk are calculated by the one-dimensional momentum theory [21–23]. To improve the accuracy of the AD model, Wu and Porté-Agel [24] incorporated the rotational effect in the AD model by using the blade element momentum (BEM) method to provide the tangential force, and improved the agreement of the AD predictions with wind tunnel measurements [25]. Shapiro et al. [26] proposed a filtered AD model in which a vortex cylinder model was employed to quantify the shedding vorticities behind the disk. Although the AD model is computational efficient, it cannot accurately predict the effect of individual blades. The AL model is more accurate by representing turbine blades using rotating lines with distributed forces, in which the forces are calculated from the blade element approach via tabulated drag and lift coefficients and the local relative wind speed [22,27–29]. Because a single point is used to represent a blade span section in the AL model, thus it cannot capture the chordwise dimension of the airfoil shape. To incorporate the chordwise dimension of the blade, the AS model is introduced, which represents the blade as zero-thickness surface formed by chords at different radial locations [30–34]. However, it is still expensive to employ the AL/AS models in wind farm simulations due to the usage of small time steps. In our previous study [35], it has been shown that the actuator disk model with uniformly distributed forces cannot accurately predict the meandering of turbine wakes, which, on the other hand, can be accurately predicted by using the actuator surface models for the blades and the nacelle as developed in Ref. [33].

In the present study, we employ the AS model developed in Ref. [33] to validate the AD model with non-uniformly distributed axial forces and tangential forces for predicting wakes from different utility-scale turbine designs. Two types of AD models (with and without the rotational effect, which are denoted as the AD-R and the AD-NR models, respectively) are considered. Three turbine designs are considered, including the EOLOS 2.5 MW wind turbine, the NREL 5 MW wind turbine and a variant of the NREL turbine, i.e., the NREL-V turbine. The axial force coefficients of the three turbine designs are featured by two types of distributions, i.e., 1) roughly uniformly distributed in the radial direction, and 2) higher near the blade root. Although studies on evaluating the actuator disk model have been carried out in the literature (e.g., Refs. [24,36,37]), to the best of our knowledge, this is the first time evaluating the predictive capability of the non-uniformly loaded actuator disk models with/without rotation for predicting the wakes of different wind turbine designs. As will be demonstrated by the simulation results, the predictive capability of the AD model is different for different wind turbine designs. While the mean velocity deficits predicted by different AD models are similar, what we want to emphasize is that the predictive capability of the AD models in the turbulence kinetic energy and Reynolds shear stress differs for different turbine designs. Specifically, the predictions of these turbulence quantities are similar between different AD models for the one with uniformly distributed axial force coefficient, while are significantly different for the others that have higher axial force near the blade root region. The simulation results further show that the actuator disk model with rotational effect considered performs better than the one without.

The rest of the paper is structured as follows. In Section 2, the employed AS and AD models are briefly introduced together with the flow solver for the large-eddy simulations in this paper. The computational setup, including the employed AS and AD meshes, is presented in Section 3. In Section 4, at different downwind positions, the results computed by the AD-NR and the AD-R models are compared with the AS predictions to evaluate the capability of the AD models in predicting wakes of different designs. At last, the conclusions are drawn in Section 5.

2. Numerical methods

In this section, numerical methods for simulating different kinds of wind turbines are briefly described, including the non-uniformly loaded actuator disk (AD) models, the flow solver employed in this work, and the actuator surface (AS) model from which the predictions are employed as the reference for evaluating the AD model.

2.1. Actuator surface model

In the actuator surface (AS) model proposed by Yang and Sotiropoulos [33], the turbine blade is represented by a zero thickness surface formed by chord lines at different radial locations [32,37]. Just like the actuator line model, the radial distributed lift $\boldsymbol{L}$ and drag force $\boldsymbol{D}$ per unit length are calculated as follows:

$$\boldsymbol{L} = \frac{1}{2}\rho c C_L U_{\text{ref}}^2 \boldsymbol{e}_L, \tag{1}$$

$$\boldsymbol{D} = \frac{1}{2}\rho c C_D U_{\text{ref}}^2 \boldsymbol{e}_D, \tag{2}$$

where ρ is the air density, C_L, C_D are the lift and the drag coefficients from a look-up table, respectively. c is the chord length at each radial position of the blade, U_{ref} is the flow velocity relative to the blade, $\boldsymbol{e}_L$ and $\boldsymbol{e}_D$ denote the unit vectors in the direction of the lift and the drag forces, respectively. In addition, the rotational effect model from Du and Selig's [38] and the tip loss effect model from Shen [22] are employed.

After calculating the lift ($\boldsymbol{L}$) and drag ($\boldsymbol{D}$) forces from Eq. (1) and (2), the total force per unit area ($\boldsymbol{f(X)}$) applied on the surface of the blade at each radial direction can be calculated by

$$\boldsymbol{f}(\boldsymbol{X}) = (\boldsymbol{L}+\boldsymbol{D})/c, \tag{3}$$

where $\boldsymbol{X}$ denotes the grid point at the actuator surface.

The actuator surface model has been systematically validated in Ref. [33] by comparing its predictions with the measured data for different turbine designs. More details of the actuator surface model can be found in Ref. [33].

2.2. Actuator disk model

The actuator disk (AD) model neglects the geometry of the rotating blade by representing it as a fixed two-dimensional porous disk, which exerts a thrust force on the incoming flow. In the present work, instead of using the one-dimensional moment method or the blade element moment method to provide the force applied on the disk for the AD model, the non-uniform thrust force and tangential force applied on the AD model are specified from the results of the AS simulations. Firstly, the AS simulation is performed with the axial force ($F_{a,AS}$) and the tangential force ($F_{t,AS}$) recorded at each time step, which are computed by projecting the lift and drag forces, i.e., $\boldsymbol{L}$ and $\boldsymbol{D}$, to the axial and tangential directions, respectively. Then, as shown in Fig. 1, these forces exerting on the three actuator surfaces in the AS model are equally distributed to the actuator disk at each radial annulus. In Fig. 1, the three blades in the AS model are shown in blue, while the porous disk is shown in black with dashed lines representing the radial annulus at r

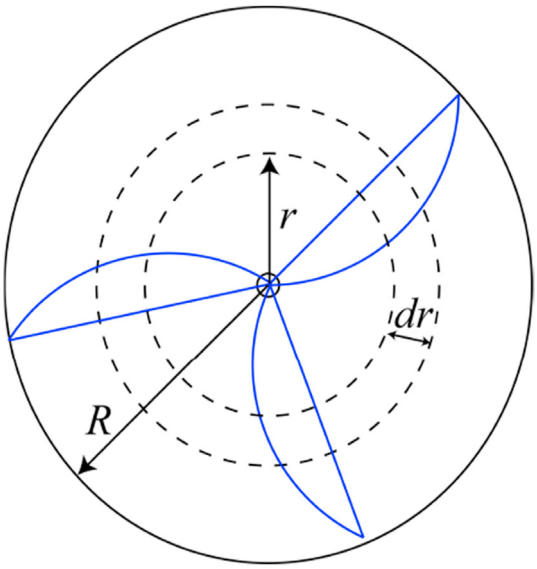

Fig. 1. Schematic for computing C_a and C_t in the Actuator Disk (AD) model from results of the Actuator Surface (AS) simulation. The blue color represents three wind blades in the AS model, the circle represents the porous disk in the AD model, and the dish lines represents the radial annulus in the AD model.

location. Equating the force exerting on the radial annulus of the actuator disk with that on the three blades from the AS simulation at radial location r, the axial force coefficient C_a and the tangential force coefficient C_t applied on the actuator disk can be computed via the following equations:

$$\frac{1}{2}\rho U_{hub}^2 2\pi r C_a dr = 3F_{a,AS} dr, \tag{4}$$

$$\frac{1}{2}\rho U_{hub}^2 2\pi r C_t dr = 3F_{t,AS} dr, \tag{5}$$

where U_{hub} is the incoming velocity at hub height. From the above two equations, the expressions for computing the axial force coefficient C_a and the tangential force coefficient C_t are obtained as follows:

$$C_a = \frac{3F_{a,AS}}{\rho\pi r U_{\text{hub}}^2}, \tag{6}$$

$$C_t = \frac{3F_{t,AS}}{\rho\pi r U_{hub}^2}. \tag{7}$$

With the obtained C_a and C_t, the axial force f_a and the tangential force f_t per unit area on the actuator disk are computed as follows:

$$f_a = \frac{1}{2}\rho U_{hub}^2 C_a, \tag{8}$$

$$f_t = \frac{1}{2}\rho U_{hub}^2 C_t, \tag{9}$$

In the present work, two actuator disk models (with and without rotational forces corresponding to AD-R and the AD-NR models, respectively) are considered. Specifically, both f_a and f_t are applied on the actuator disk in the AD-R model, while the tangential force f_t is set as zero in the AD-NR model. It is noted that in both the AS and the AD simulations, the nacelle is modeled by using the AS model of Yang and Sotiropoulos [33]. The forces computed using the AD/AS model are distributed to the fluid background grid nodes using the smoothed delta function, which is widely used in the immersed boundary method to simulate fluid-structure interactions [39–42]

2.3. Flow solver

The large-eddy simulation (LES) module of the VFS-Wind code [29] is employed in the present work to solve the three-dimensional filtered Navier-Stokes equations in the following form:

$$J\frac{\partial U^i}{\partial \xi^i} = 0, \tag{10}$$

$$\frac{1}{J}\frac{\partial U^i}{\partial t} = \frac{\xi_l^i}{J}\left(-\frac{\partial}{\partial \xi^j}\left(U^j u_l\right) + \frac{\mu}{\rho}\frac{\partial}{\partial \xi^j}\left(\frac{g^{jk}}{J}\frac{\partial u_l}{\partial \xi^k}\right) - \frac{1}{\rho}\frac{\partial}{\partial \xi^j}\left(\frac{\xi_l^j p}{J}\right) - \frac{1}{\rho}\frac{\partial \tau_{lj}}{\partial \xi^j} + f_l\right), \tag{11}$$

where $i, j, k, l = 1, 2, 3$, x_i is the Cartesian coordinates, ξ^i are the curvilinear coordinates, $\xi_l^i = \frac{\partial \xi_i}{\partial x_l}$ is the transformation metrics, J is the Jacobian of the geometric transformation, $U^i = (\xi_l^i/J)u_l$ is the contravariant volume flux, u_i is the ith component of velocity vector in Cartesian coordinates, μ is the dynamic viscosity, $g^{jk} = \tau_l^j \tau_l^k$ is the components of the contravariant metric tensor, p is the pressure, f_l is the body force resulted from the turbine blade and nacelle computed using the actuator surface/disk models, τ_{ij} is the sub-grid stress (SGS) tensor introduced by the filtering operation modeled using the Smagorinsky SGS model [43] as fellows:

$$\tau_{ij} - \frac{1}{3}\tau_{kk}\delta_{ij} = -\mu_t \overline{S_{ij}}, \tag{12}$$

where the $\bar{\cdot}$ represents the grid filtering operator. S_{ij} is the large-scale strain rate tensor, the μ_t is the eddy viscosity computed by

$$\mu_t = C_s \Delta^2 |\overline{S}|, \tag{13}$$

where Δ denotes the filter width, C_s is the Smagorinsky constant computed via the dynamic procedure [44], and $|\overline{S}| = \sqrt{2\overline{S_{ij}}\overline{S_{ij}}}$ is the magnitude of the strain-rate tensor.

A second-order accurate central difference scheme is applied to discretize the governing equation in space, and the fractional step method [45] is used for temporal integration. A matrix-free Newton–Krylov method [46] is employed to solve the momentum equation, meanwhile the Generalized Minimal Residual (GMRES) method along with an algebraic multi-grid acceleration is employed to solve pressure Poisson equation [47].

3. Computational setup

Here different wind turbine designs are considered: 1) The EOLOS wind turbine, a Clipper Liberty C96 2.5 MW wind turbine installed at the EOLOS wind energy research field station at University of Minnesota; 2) the NREL 5 MW wind turbine, a reference offshore baseline wind turbine developed at NREL; 3) a variant of the NREL wind turbine, i.e., NREL-V, which is designed based on the NREL turbine using an inverse design method [48,49], with its chord and twist distributions presented in the Appendix A. The rotor of the EOLOS turbine is $D = 96$ m positioned at the hub height

of $z_{hub} = 80$ m and the nacelle is of size 5.3 m × 4.7 m × 5.5 m. More information about this turbine can be found from previous studies [50–52]. The rotor diameters of the NREL and the NREL-V turbines are both $D = 126$ m with the hub of the rotor located at $z_{hub} = 90$ m. More specifics of the NREL turbine design can be found in Refs. [53,54]. In this study, a 16 m × 5 m × 5 m cuboid nacelle is used for the NREL and the NREL-V turbines.

For all the cases, the same computational set up shown in Fig. 2 is employed, in which the x, y and z are the streamwise, the spanwise and the vertical directions, respectively. The size of the domain is $L_x \times L_y \times L_z = 14D \times 7D \times 10D$ discretized with a Cartesian grid of $N_x \times N_y \times N_z = 281 \times 281 \times 143$. The computational domain is chosen in a way that the streamwise length is enough to cover the wake locations of interest in this work, the spanwise length is large enough to avoid the effect of the spanwise boundary on the wake evolution, and the vertical height (approximately 1 km) is comparable to the thickness of atmospheric boundary layer. Computational domains of similar sizes have been employed in the literature [16,37]. The turbine is located at $3.5D$ from the inlet. At the inlet, the uniform inflow is applied. At the outlet, the Neumann boundary condition is applied. On the other four boundaries, the free-slip boundary conditions is employed. The mesh is uniformly distributed in x and y directions with grid size $\Delta x = D/20$ and $\Delta y = D/40$, respectively. In the vertical direction, the mesh is uniform with $\Delta z = D/40$ within $z = (0, 2D)$ region and gradually stretches to the top boundary. Grid refinement study has been carried out in our previous work [16], which showed that the employed mesh is enough for predicting the quantities of interest in this work. The time steps for the AS and AD simulations are $0.00417D/U_{hub}$ and $0.00833D/U_{hub}$ in the EOLOS turbine case and $0.00317D/U_{hub}$ and $0.00635D/U_{hub}$ in the NREL and NREL-V turbine cases, respectively. Smaller time step is employed in the AS simulation to ensure that the tip of the blade does not pass more than one grid spacing in one time step. Fig. 3 shows the meshes discretizing the actuator surface and actuator disk for the EOLOS and NREL turbines. As seen, the unstructured triangular mesh is used. For the EOLOS turbine case, the numbers of triangle elements are 376, 3042 and 2370 for the nacelle mesh, the actuator surface mesh and the actuator disk mesh, respectively. For the NREL and NREL-V turbine cases, 532, 3042 and 2370 triangular elements are employed to discretize the nacelle, the actuator surface and actuator disk, respectively. In turbine cases, the incoming streamwise velocity at the hub height of the rotor is $U_{hub} = 8$ m/s. The Reynolds number $\mathrm{Re} = DU_{hub}/\nu = 5.67 \times 10^8$ for all cases, where ν is the kinematic viscosity. In the AS and simulation for all turbines, the tip speed ratio is set to be eight (TSR = 8.0), which is the ratio between the tangential speed of the blade tip and the incoming wind speed at hub position U_{hub} shown as follows:

$$\mathrm{TSR} = \frac{\Omega R}{U_{\mathrm{hub}}}, \tag{14}$$

where Ω is the rotational speed of the rotor, R is the rotor radius. To confirm the findings from this work, cases with a different value of TSR are also carried out with the simulation results presented in Appendix C.

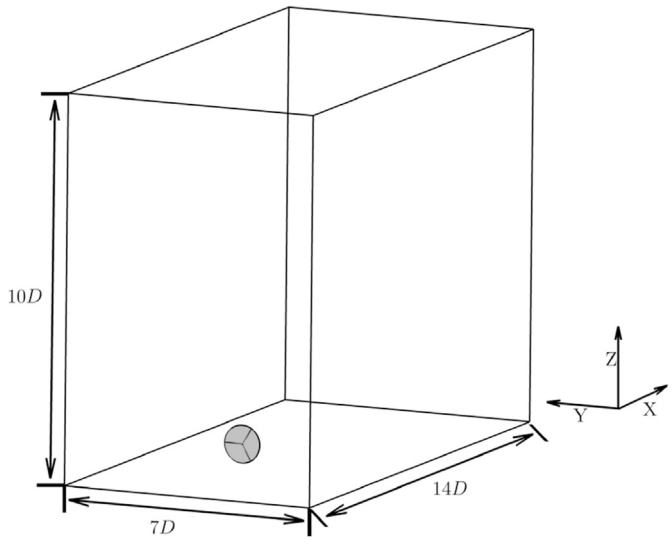

Fig. 2. Schematic of the computational domain, where x, y and z denote the streamwise, the spanwise and the vertical directions, respectively. The turbine is located at $3.5D$ from the inlet, where D is the rotor diameter.

4. Results and discussion

In this section, at the tip speed ratio of eight, the results from the simulation of the EOLOS, the NREL and the NREL-V turbines using the AS, the AD-R and the AD-NR models are presented and discussed. Please note that U, V and W denote the time-averaged velocity components in the streamwise, the spanwise and the vertical directions, respectively.

Before comparing the flow field in turbine wake, Fig. 4 plots the radial distributions of C_a and C_t obtained from the actuator surface (AS) simulations of the EOLOS, the NREL and the NREL-V turbine designs. As seen, the C_a from the NREL turbine is more evenly distributed in the range of 0.2–0.9 r/R when compared with that from the EOLOS turbine, which shows a sharp increase to approximately 1.17 at $r/R \approx 0.3$ and abruptly decrease to zero as approaching the blade tip region. We suspect that the different distributions of C_a in the region near the blade root are the reason for different predictive capabilities of the AD model for these two different turbine designs. Therefore, simulations of the newly designed NREL-V turbine which shows higher C_a distribution near the blade root region are conducted. The detailed flow field will be discussed and presented in the following section. On the other hand, the overall shape of the distribution of the C_t is similar for all turbine designs, although some differences are observed in terms of the locations where the maximum and minimum C_t. The averaged C_as for the EOLOS, the NREL and the NREL-V turbine are 0.638, 0.684 and 0.654, respectively.

In this section, we compare the simulation results from the AD-R and AD-NR models with those from the AS model for all turbines, i.e., the EOLOS, the NREL, and the NREL-V turbines. At different downwind positions in the horizontal rotor plane $x - y$ plane at $z = z_{hub}$, Figs. 5–7 plot the time-averaged streamwise profiles of velocity U, the turbulent kinetic energy k and the Reynolds shear stress $\langle u'v' \rangle$ from $-1D$ to $1D$ of the spanwise direction, respectively. Besides, the first, second and third rows are results of the EOLOS, the NREL and the NREL-V turbines, respectively. For all turbine designs, it is observed from Fig. 5 that the streamwise velocity profiles predicted by the AD-R model show well agreement with the results obtained by the AS model starting from the near wake region ($x = 1D$) until $9D$ downwind of the turbine. However, velocity deficits predicted by the AD-NR display somewhat differences. Specifically, the AD-NR model predicts well in the NREL turbine case from $1D$ to $9D$ downwind regions, and same results shown in the NREL-V turbine case expect at far wake region ($9D$). However, for the EOLOS, the velocity computed by the AD-NR model is smaller than that of the AS and AD-R models from range $1D$ to $9D$. The different predicative capability of the AD-NR model in simulation different turbine designs indicates that the EOLOS

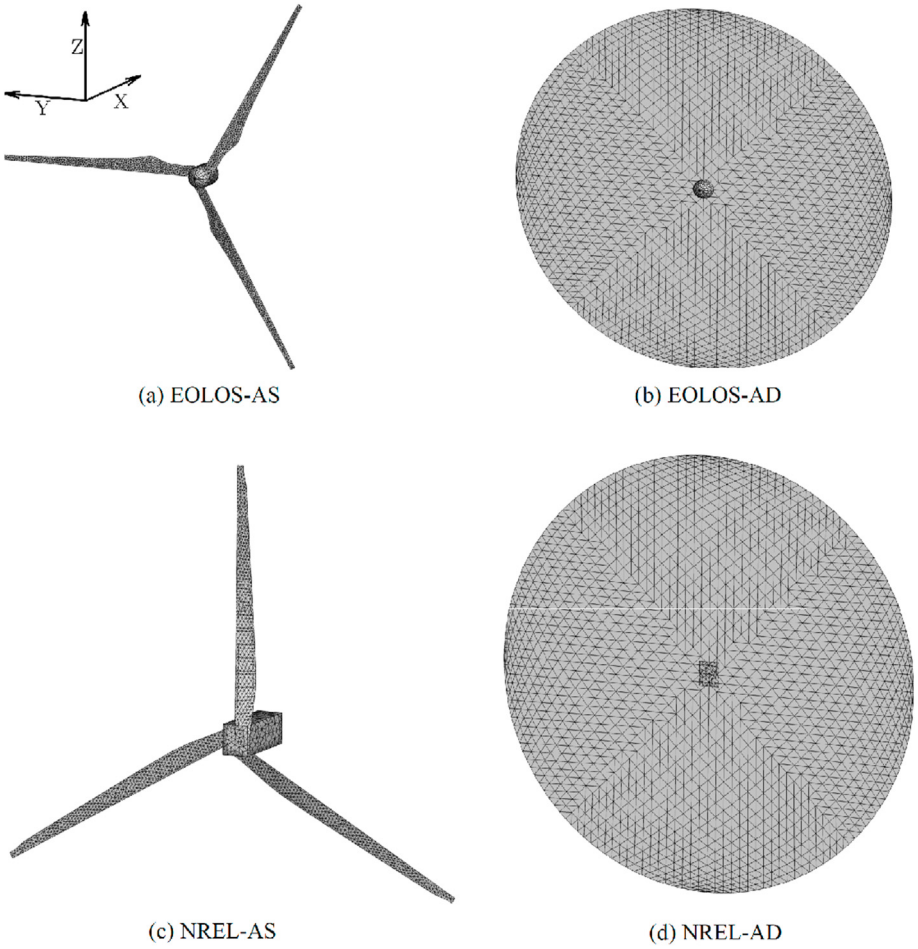

Fig. 3. The unstructured triangular mesh of the AS and the AD models for (*a*) the AS mesh of the EOLOS turbine, (*b*) the AD mesh of the EOLOS turbine, (*c*) the AS mesh of the NREL turbine, and (*d*) the AD mesh of the NREL turbine.

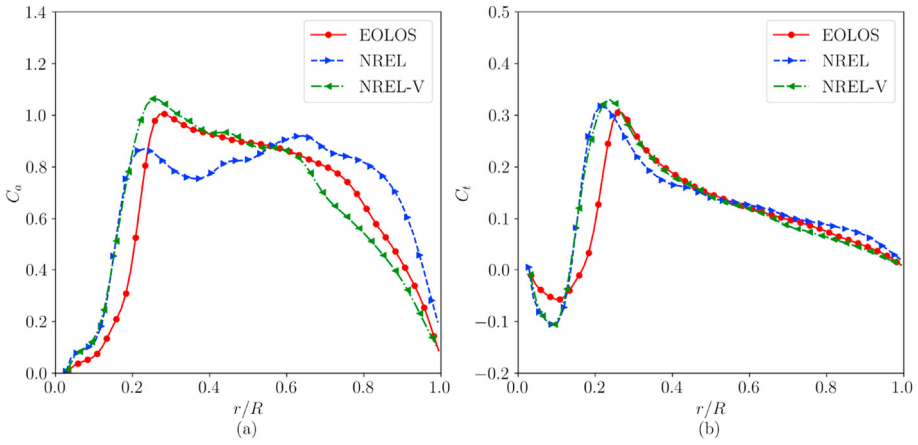

Fig. 4. The distributions of the axial force coefficient (C_a) and tangential force coefficient (C_t) along the blade axial direction. Solid red lines with circles: the EOLOS turbine; Dashed blue lines with right triangles: the NREL turbine; Dashed dot green lines with left triangles: the NREL-V turbine.

turbine experiences stronger rotational effects for near wake to far wake compared to the NREL and the NREL-V turbine designs.

The comparison of the turbulent kinetic energy k shown in Fig. 6 illustrates that for the NREL turbine, the prediction of the AD models agrees well with the results of the AS model from 1D to 9D downwind position except at $x = 3D$ location, at which the TKE predicted by the AD models is less than the AS model. In the case of the NREL-V turbine, the AD models predict well from 1D to 3D, After that, the AD models predict less k compared with results of the AS model, and the less k is predicted by the AD-NR model

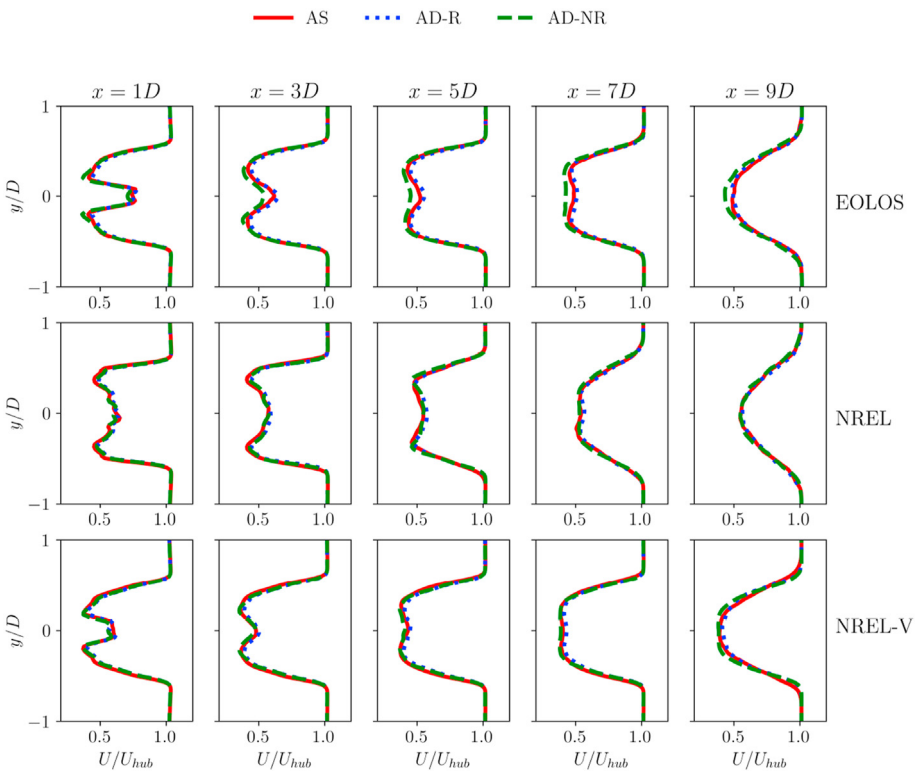

Fig. 5. Profiles of the streamwise velocity U for (a) the EOLOS turbine, (b) the NREL turbine, and (c) the NREL-V turbine in the horizontal $x - y$ plane at $z = z_{hub}$ at different downwind positions.

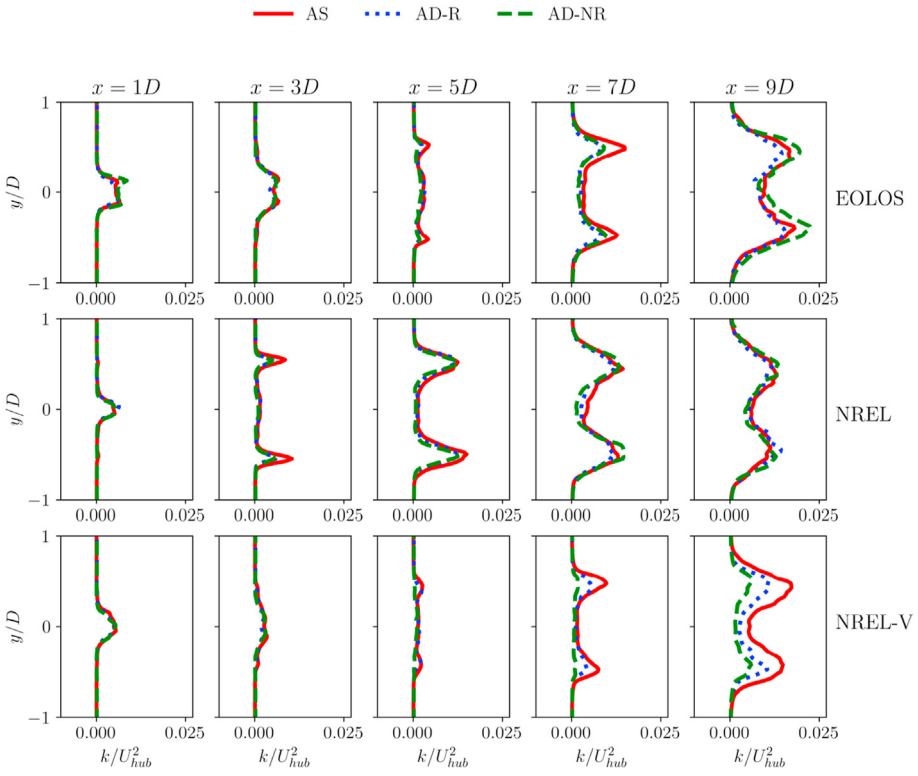

Fig. 6. Profiles of the turbulent kinetic energy k for (a) the EOLOS turbine, (b) the NREL turbine, and (c) the NREL-V turbine in the horizontal $x - y$ plane at $z = z_{hub}$ at different downwind positions.

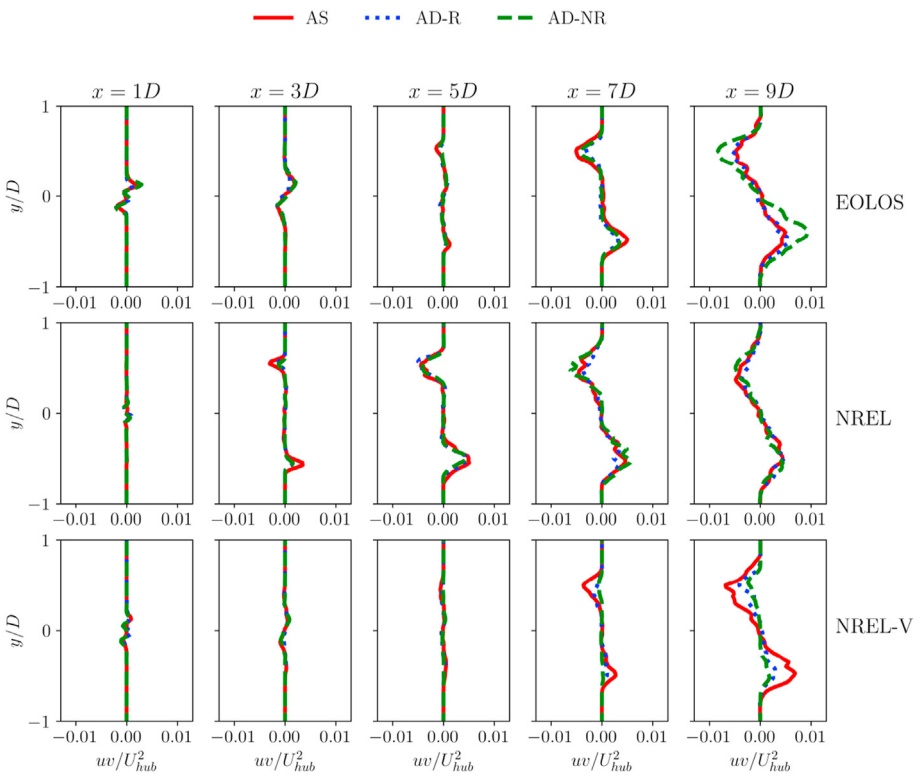

Fig. 7. Profiles of the Reynolds stress $\langle u'v' \rangle$ for (a) the EOLOS turbine, (b) the NREL turbine, and (c) the NREL-V turbine in the horizontal $x - y$ plane at $z = z_{hub}$ at different downwind positions.

compared with the AD-R model. However, the AD models show different predictive capability in simulating the EOLOS turbine. Specifically, the AD models do not predict well from near to far wake regions. At $x = 1D$ and $x = 9D$ the AD-R model predicts less k while the AD-NR model predicts more k in comparison with results of the AS model. From $x = 3D$ to $x = 7D$ wake regions, the results of the AD-NR and AD-R models show well agreement while the results predicted by them are less than that of the AS model.

Then, the Reynolds shear stress $\langle u'v' \rangle$ computed by the AD and AS models for different turbine designs is compared in Fig. 7. For the NREL turbine, the results of the AD models agree well with that of the AS model, and only slight difference can be seen. In the case of the EOLOS turbine, the AD-R model predicts well from $x = 1D$ to $x = 9D$ regions, however the AD-NR model predicts well in the near wake from $1D$ to $7D$, but over-predicts at the far wake region at $x = 9D$. Similar for the NREL-V case, the AD-R model predicts well from $1D$ to $7D$ downwind of the turbine, and only a slight difference appears in the $9D$ region. Meanwhile the AD-NR model predicts well from $1D$ to $5D$, and it under-predicts $\langle u'v' \rangle$ from $7D$ to $9D$ regions.

Fig. 8 shows contours of the turbulent kinetic energy k and the Reynolds shear stress $\langle u'v' \rangle$. For all the turbines, it is seen that the regions with high turbulent kinetic energy and larger magnitudes of Reynolds shear stress appear in the near hub region located immediately behind wind turbine and in the tip shear layer located in the far wake, respectively. The hub induced turbulent kinetic energy k appears immediately behind the turbine, and stronger k can be seen until approximately $5D$, $2D$ and $6D$ downwind positions in the case of the EOLOS, NREL and NREL-V turbines, respectively. Meanwhile, the shear induced Reynolds shear stress $\langle u'v' \rangle$ appears at $4D$, $2D$ and $6D$ downwind positions in the case of the EOLOS, NREL and NREL-V turbines, respectively. Besides, for all cases, the turbulent kinetic energy k and the Reynolds shear stress $\langle u'v' \rangle$ appear early in the results of the AS model than that of the AD models.

The POD analysis of the spanwise velocity fluctuations, a good indicator for the spanwise motion of the wake, is carried out for the three different turbine designs. For all cases, 6000 snapshots are used in the POD analysis. Fig. 9 shows the percentage of energy contained in each POD mode for different turbine designs. As seen from the AS results, the overall trends are different for different turbine designs. More energy concentrated in the first two POD modes for the NREL-V turbine. As for the comparison between the AD and the AS results, differences are observed for a wide range of POD modes for the NREL turbine, but only for the first several modes of the EOLOS and the NREL-V turbines.

Fig. 10 shows the 1st, 3rd and 5th POD modes from the simulations of the EOLOS, the NREL and the NREL-V turbines. We first compare the POD modes from different turbine designs. As seen, the locations and the patterns of the POD modes are different for different turbines designs. Organized POD patterns appear at about $6D$ downwind of the turbine for the EOLOS and NREL-V turbine design, which, on the other hand, starts at $3D$ downwind for the NREL turbine. The streamwise extent of the patterns in the wake of the NREL turbine is observed being smaller than the other two turbine designs. For the three POD modes considered here, four different patterns can be identified, i.e., 1) continuous straight shape of the same sign in the upper (positive y) and lower (negative y) parts of the wake; 2) continuous deformed shape of the same sign in the upper and lower parts of the wake; 3) discontinuous shape of the different sign in the upper and lower parts of the wake; and 4) irregular shape with non-periodic sign changes. For the EOLOS turbine, the 1st mode is mainly composed of pattern 3 for AS, AD-R and AD-NR models, while slight differences appears that pattern 1 starts in the far wake at $x \approx 9D$ for the AD-R and AD-NR models. For the 1st mode of the NREL turbine, pattern 1 starts from

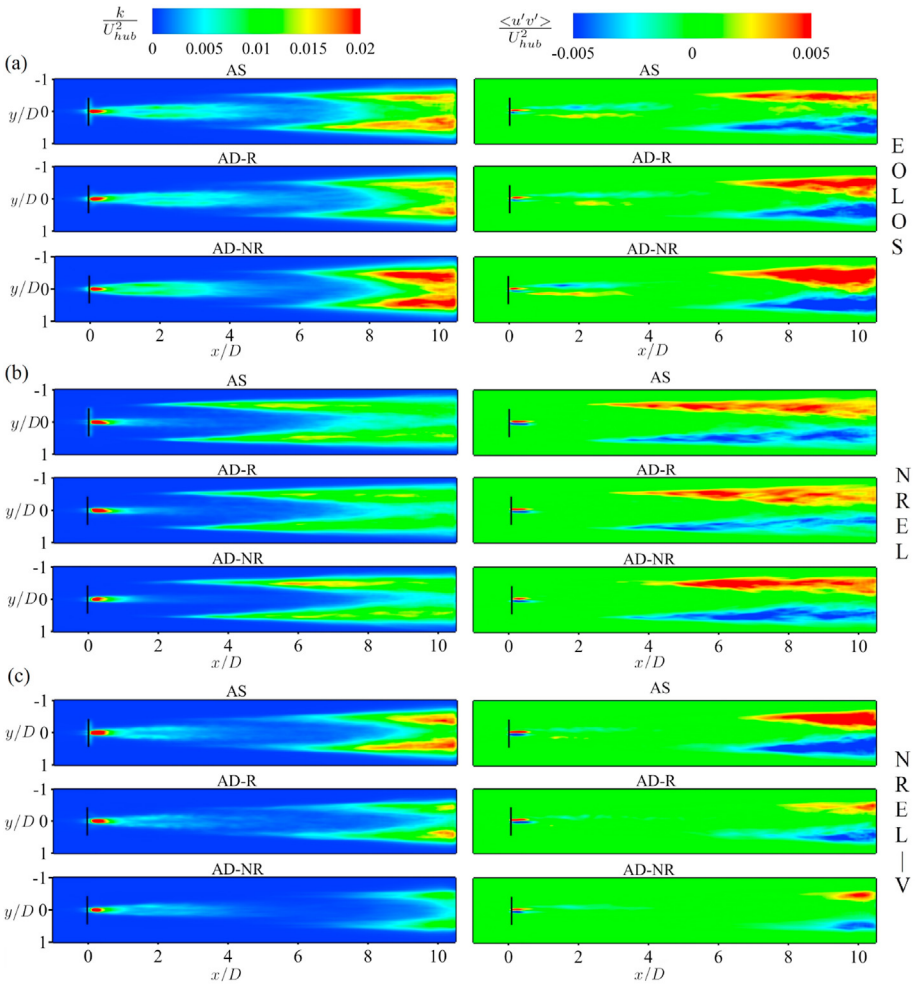

Fig. 8. Contours of the turbulent kinetic energy k (left) and the Reynolds stress $\langle u'v' \rangle$ (right) for (a) the EOLOS turbine, (b) the NREL turbine, and (c) the NREL-V turbine in the horizontal $x - y$ plane at $z = z_{hub}$ at different downwind positions.

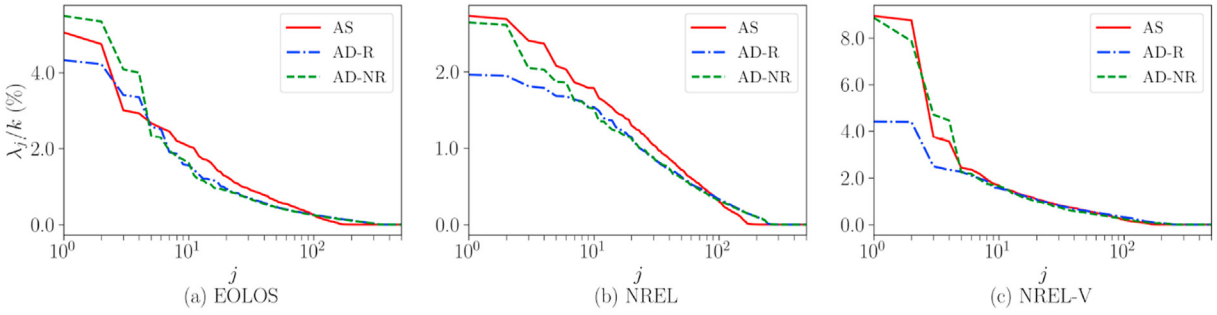

Fig. 9. POD mode energy of the normalized spanwise velocity v/U_{hub} plotted here for the first 500 modes for the (a) EOLOS, (b) NREL and (c) NREL-V turbines. These energy is normalized by the total kinetic energy k for each case.

3D, then changes to pattern 2 and pattern 3 at far wake locations in the AS results. Differences between the AD-R and AS predictions of mode 1 are observed for the NREL turbine, that in the AD-R results significant patterns are observed at relatively further wake locations with a narrower region with pattern 1. If the rotation is not considered, more differences are observed in mode 1 of the NREL turbine, which is wider in the streamwise direction and is mainly composed of mode 1 at the far wake locations. For mode 1 of the NREL-V turbine, the overall patterns predicted by the three different models are similar with each other, with that from the AD-R model starting at somewhat further downwind locations and less organized. For modes 3 and 5 of the NREL turbine, the predictions from different AD models are similar with the AS predictions. As for the NREL turbine, some differences between AD and AS models are observed especially for mode 5, for which the size of the pattern from the AS model is larger than the other two models. For mode 3 and mode 5 of the NREL-V turbine, on the other hand, the patterns predicted by the AD-R models are quite different from the AS

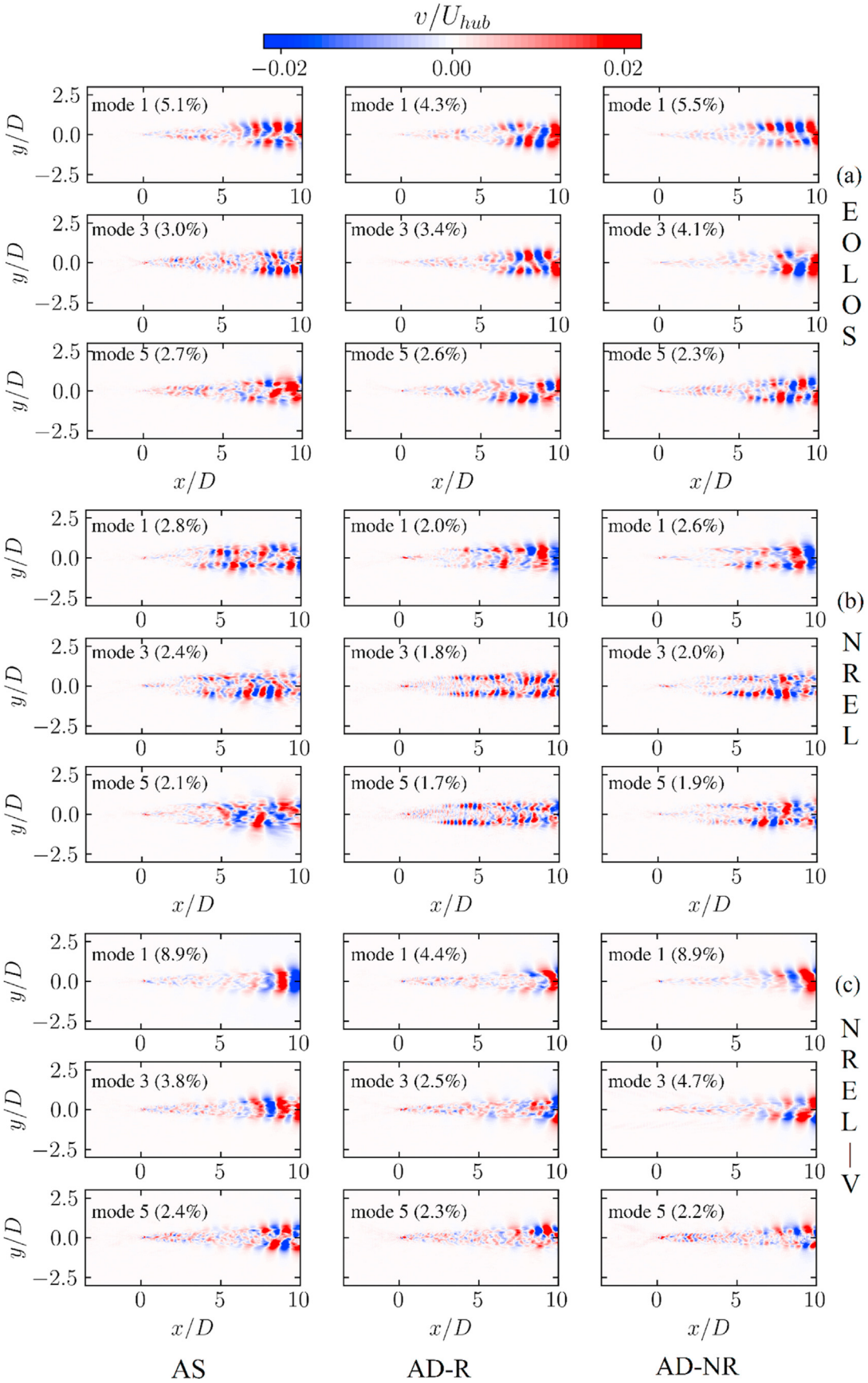

Fig. 10. Contours of the 1st, 3rd and 5thPOD modes of the normalized spanwise velocity v/U_{hub} for the (a) EOLOS, (b) NREL and (c)NREL-V turbines. Results of the AS, AD-R and AD-NR models are presented in the first, second and third columns, respectively.

model.

5. Conclusions

In this study, the capability of the AD model in predicting turbine wakes of different blade designs is evaluated by comparing the AD predictions of the 2.5 MW EOLOS wind turbine, the 5 MW NREL wind turbine and a variant of the NREL wind turbine (NREL-V) with the AS predictions. The wake turbulence is simulated using large eddy simulation. Two different AD models with and without the rotational effect (i.e., AD-R and AD-NR) are considered. In the AD models, the radial distributions of the axial and tangential (AD-R only) force coefficients are computed using the AS simulation results by uniformly distributing the forces to the annulus on the actuator disk at the same radius.

The simulation results show different predictive capabilities of the AD models for different wake statistics in the case of different wind turbine designs. For the streamwise velocity deficits, the predictions from the AD models are in good agreement with those from the AS model. For the turbulent kinetic energy and the Reynolds shear stress, the predictive capabilities are observed being different for different turbine designs. Specifically, good agreements between the AD predictions and the AS predictions are observed for the NREL turbine, while discrepancies are observed for the EOLOS and the NREL-V turbines. The comparisons of the POD modes between the AD and AS predictions, on the other hand, are complex. The patterns of the POD modes predicted by the AD-R model are in general agree better with the AS results when compared with the AD-NR model. However, discrepancies are also observed in terms of the location and the details of the POD patterns.

The different predictive capabilities of the AD models for different turbine designs are associated with different radial distributions of the axial force. For the NREL turbine design, the axial force coefficient are evenly distributed at most radial locations. For the EOLOS and NREL-V turbine designs, on the other hand, the axial force coefficients are larger near the root of the blade while they are smaller near the tip of the blade. Such different distributions of the axial force cause different instability mechanism of the wake. For the NREL turbine, the radial gradient of the streamwise velocity deficit is high near the tip region that the instability of the wake starts from the tip region as demonstrated by the POD modes. For the EOLOS and NREL-V turbine designs, on the other hand, the wake instability is induced by the interaction between the hub vortex and the outer shear layer at far wake locations as the hub vortex grows in radius when traveling downwind.

CRediT authorship contribution statement

Guodan Dong: Conceptualization, Investigation, Methodology, Software, Writing – original draft. **Zhaobin Li:** Conceptualization, Methodology, Software, Writing – review & editing. **Jianhua Qin:** Methodology, Writing – review & editing. **Xiaolei Yang:** Conceptualization, Methodology, Software, Supervision, Writing – review & editing.

Declaration of competing interest

The authors declare that they have no known competing financial interests or personal relationships that could have appeared to influence the work reported in this paper.

Acknowledgement

This work was supported by National Natural Science Foundation of China (NO. 11988102, 12172360). Qin was supported by China Postdoctoral Science Foundation (NO. 2021M693241).

Appendix A

In this appendix, we compare the distributions of twist and chord of the NREL-V turbine with those of the NREL turbine. As seen in Fig. 11, near the hub the blade of the NREL-V turbine has a larger chord and is less twisted, while near the tip the blade has a smaller chord and is more twisted when compared with the NREL turbine. It is note, the thrust force coefficient of the NREL-V turbine is not exactly the same as that of the NREL turbine, with the difference less than 10%.

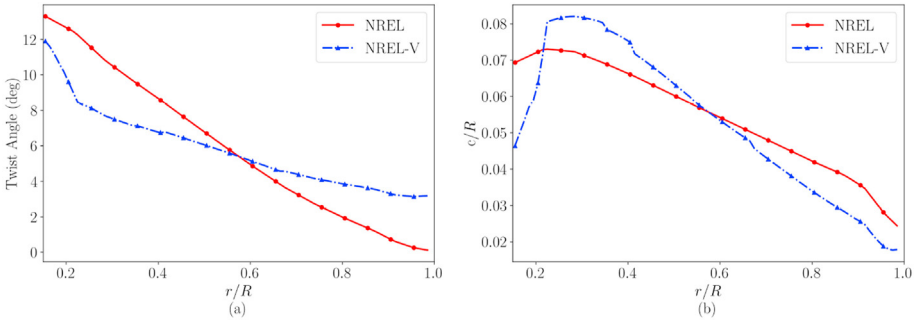

Fig. 11. Distributions of (a) twist and (b) chord of the NREL turbine and the NREL-V turbine.

Appendix B

The proper orthogonal decomposition (POD), also known as Karhunen–Loève procedure [55,56], could identify the most energetic structures from complex fluid flow. To deal with our 3D wind turbine simulation results, the snapshot POD method is adopted because of its computational efficiency. A brief introduction of the snapshot POD algorithm is given as follows:

Step 1: Collecting data.

For a series of time steps, the flow field velocities are stacked in terms of a collection of the column vector $\boldsymbol{q}(\boldsymbol{x}, t)$ which represents the velocity fluctuating and is defined as follows:

$$\boldsymbol{q}(\boldsymbol{x},t) = \boldsymbol{u}(\boldsymbol{x},t) - \boldsymbol{U}(\boldsymbol{x}) = \sum_{j=1}^{\infty} a_j(t)\boldsymbol{\varphi}_j(\boldsymbol{x}). \tag{15}$$

Step 2: Constructing the correlation matrix R.

$$R = \frac{1}{n}\sum_{j=1}^{n} \boldsymbol{q}^T(t_j)\boldsymbol{q}(t_j) = Q^T Q \in \mathbb{R}^{m\times m}, \tag{16}$$

where the matrix Q represents the m snapshots data of flow velocities being stacked as:

$$Q = [\boldsymbol{q}(t_1) \quad \boldsymbol{q}(t_2) \quad \dots \quad \boldsymbol{q}(t_m)] \in \mathbb{R}^{n\times m}, \tag{17}$$

where n is the number of grid points and m is the number of time series. In our 3D simulations, n is extremely large (approximately 11 million) compared with $m = 6000$, the snapshot POD method is therefore adopted. Specifically, the eigenvalue problem of a smaller correlation matrix C with size $(m \times m)$ (shown in Eq. (17)) is solved, instead of solving the eigenvalue of a classical correlation matrix QQ^T with size $(n \times n)$ in the classical POD method.

Step 3: Computing eigenvalues.

The eigenvalue of Q is solved as:

$$R\boldsymbol{\varphi}_j = \lambda_j \boldsymbol{\varphi}_j, \quad \boldsymbol{\varphi}_j \in \mathbb{R}^m \tag{18}$$

where $\boldsymbol{\varphi}_j$ with $k = 1, 2, \dots, m$ denotes number of the orthogonal POD modes. The strength of the jth POD mode is λ^j which represents the mode's relative contribution to the turbulent kinetic energy (TKE, k).

$$k = \sum_{j=1}^{n} \lambda_j. \tag{19}$$

The eigenvectors of the classical POD analysis can be determined as follows:

$$\boldsymbol{\psi}_j = X\boldsymbol{\varphi}_j \frac{1}{\sqrt{\lambda_j}} \in \mathbb{R}^n. \tag{20}$$

Equivalently:

$$\Psi = X\Phi\Lambda^{-1/2}. \tag{21}$$

It should be noted that $\Psi = [\boldsymbol{\psi}_1 \quad \boldsymbol{\psi}_2 \quad \cdots \quad \boldsymbol{\psi}_m] \in \mathbb{R}^{n\times m}$ and $\Phi = [\boldsymbol{\varphi}_1 \quad \boldsymbol{\varphi}_2 \quad \cdots \boldsymbol{\varphi}_m \quad] \in \mathbb{R}^{m\times m}$.

Appendix C

In this appendix, the results from the cases with TSR = 6 are presented to demonstrate that the same conclusions can be drawn for different turbine operational conditions. In the these cases, the NREL and NREL-V turbine designs are considered with the same simulation setup as that for TSR = 8. The radial distributions of the axial force coefficient and the tangential force coefficient are shown in Figure 12. The profiles of the streamwise velocity, the turbulent kinetic energy, and the Reynolds stress for the AD-R and AD-NR cases are compared with those from the AS case as shown in Figures 13, 14 and 15, respectively. It is seen that the NREL-V turbine design gives higher thrust force coefficient C_a in the root region in comparison with the NREL turbine design. The streamwise velocity is well predicated by both the AD-R and the AD-NR models for both NREL and NREL-V turbine designs, while the turbulent kinetic energy and the magnitude of the primary Reynolds shear stress are underpredicted by the AD models (especially for the AD-NR model), which is consistent with those observed for the cases with TSR = 8.

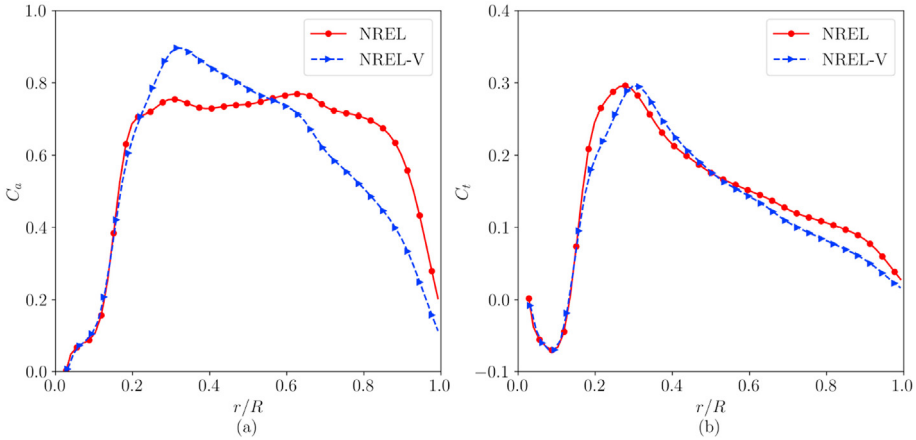

Fig. 12. The distributions of the axial force coefficient (C_a) and tangential force coefficient (C_t) along the blade axial direction at TSR = 6. Solid red lines with circles: the NREL turbine design; Dashed blue lines with right triangles: the NREL-V turbine design.

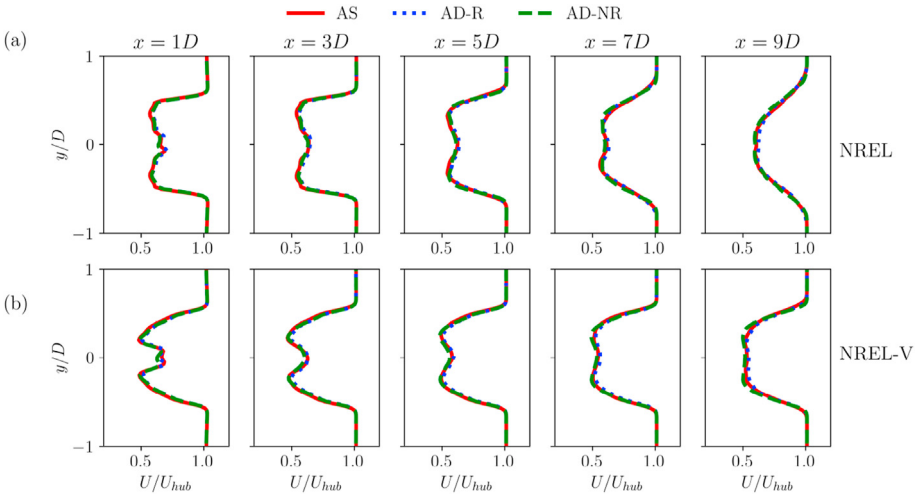

Fig. 13. Profiles of the streamwise velocity U for (a) the NREL turbine and (b) the NREL-V turbine in the horizontal $x - y$ plane at $z = z_{hub}$ at different downwind positions for the cases with TSR = 6.

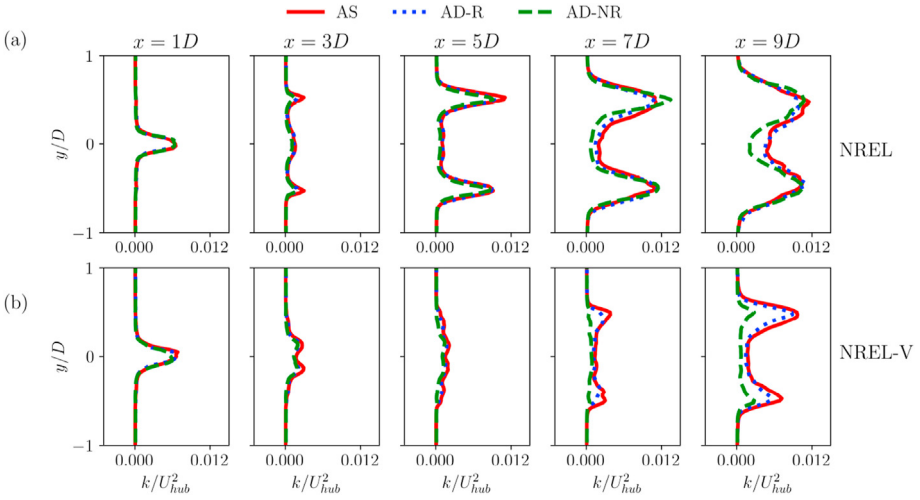

Fig. 14. Profiles of the turbulent kinetic energy k for (a) the NREL turbine and (b) the NREL-V turbine in the horizontal $x - y$ plane at $z = z_{hub}$ at different downwind positions for the cases with TSR = 6.

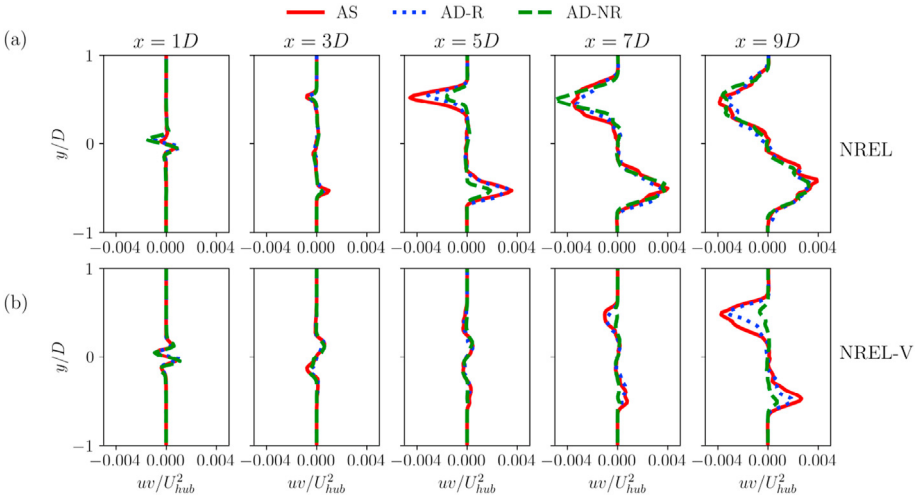

Fig. 15. Profiles of the Reynolds stress $\langle u'v' \rangle$ for (a) the NREL turbine and (b) the NREL-V turbine in the horizontal $x - y$ plane at $z = z_{hub}$ at different downwind positions for the cases with TSR = 6.

References

[1] P. Veers, K. Dykes, E. Lantz, S. Barth, C.L. Bottasso, O. Carlson, A. Clifton, J. Green, P. Green, H. Holttinen, et al., Grand challenges in the science of wind energy, Science 366 (6464) (2019), eaau2027.

[2] C. Meneveau, Big wind power: seven questions for turbulence research, J. Turbul. 20 (1) (2019) 2–20.

[3] R.J. Stevens, C. Meneveau, Flow structure and turbulence in wind farms, Annu. Rev. Fluid Mech. 49 (2017) 311–339.

[4] B. Sanderse, S. Van der Pijl, B. Koren, Review of computational fluid dynamics for wind turbine wake aerodynamics, Wind Energy 14 (7) (2011) 799–819.

[5] R.J. Barthelmie, K. Hansen, S.T. Frandsen, O. Rathmann, J. Schepers, W. Schlez, J. Phillips, K. Rados, A. Zervos, E. Politis, et al., Modelling and measuring flow and wind turbine wakes in large wind farms offshore, Wind Energy: An International Journal for Progress and Applications in Wind Power Conversion Technology 12 (5) (2009) 431–444.

[6] I. Katic, J. Højstrup, N.O. Jensen, A simple model for cluster efficiency, in: European Wind Energy Association Conference and Exhibition, vol. 1, 1986, pp. 407–410.

[7] G.C. Larsen, A Simple Wake Calculation Procedure, Risø National Laboratory, 1988.

[8] G.C. Larsen, H. Aagaard Madsen, F. Bingöl, Dynamic Wake Meandering Modeling (2007).

[9] M. Bastankhah, F. Porté-Agel, A new analytical model for wind-turbine wakes, Renew. Energy 70 (2014) 116–123.

[10] T. Kim, S. Oh, K. Yee, Improved actuator surface method for wind turbine application, Renew. Energy 76 (2015) 16–26.

[11] X. Yang, K.B. Howard, M. Guala, F. Sotiropoulos, Effects of a three-dimensional hill on the wake characteristics of a model wind turbine, Phys. Fluids 27 (2) (2015), 025103.

[12] X. Yang, M. Pakula, F. Sotiropoulos, Large-eddy simulation of a utility-scale wind farm in complex terrain, Appl. Energy 229 (2018) 767–777.

[13] T. Cai, S. Cheng, A. Segalini, L.P. Chamorro, Local topography-induced pressure gradient effects on the wake and power output of a model wind turbine, Theor. Appl. Mech. Lett. 11 (5) (2021) 100297.

[14] S. Zhang, H. Yang, B. Du, M. Ge, Effects of a rooftop wind turbine on the dispersion of air pollutant behind a cube-shaped building, Theor. Appl. Mech. Lett. 11 (5) (2021) 100296.

[15] M.F. Howland, J. Bossuyt, L.A. Martínez-Tossas, J. Meyers, C. Meneveau, Wake structure in actuator disk models of wind turbines in yaw under uniform inflow conditions, J. Renew. Sustain. Energy 8 (4) (2016), 043301.

[16] Z. Li, X. Yang, Large-eddy simulation on the similarity between wakes of wind turbines with different yaw angles, J. Fluid Mech. 921 (2021) A11.

[17] W.J.M. Rankine, On the mechanical principles of the action of propellers, Trans. Inst. Nav. Archit. (1865) 6.

[18] R.E. Froude, On the part played in propulsion by differences of fluid pressure, Trans. Inst. Nav. Archit. 30 (1889) 390.

[19] X. Yang, S. Kang, F. Sotiropoulos, Computational study and modeling of turbine spacing effects in infinite aligned wind farms, Phys. Fluids 24 (11) (2012) 115107.

[20] D. Yang, C. Meneveau, L. Shen, Large-eddy simulation of offshore wind farm, Phys. Fluids 26 (2) (2014), 025101.

[21] M. Calaf, C. Meneveau, J. Meyers, Large eddy simulation study of fully developed wind-turbine array boundary layers, Phys. Fluid. 22 (1) (2010), 015110.

[22] W.Z. Shen, J.N. Sørensen, R. Mikkelsen, Tip loss correction for actuator/Navier–Stokes computations, J. Sol. Energy Eng. 127 (2) (2005) 209–213.

[23] J.T. Conway, Exact actuator disk solutions for non-uniform heavy loading and slipstream contraction, J. Fluid Mech. 365 (1998) 235–267.

[24] Y.-T. Wu, F. Porté-Agel, Large-eddy simulation of wind-turbine wakes: evaluation of turbine parametrisations, Boundary-Layer Meteorol. 138 (3) (2011) 345–366.

[25] L.P. Chamorro, F. Porté-Agel, Effects of thermal stability and incoming boundary-layer flow characteristics on wind-turbine wakes: a wind-tunnel study, Boundary-Layer Meteorol. 136 (3) (2010) 515–533.

[26] C.R. Shapiro, D.F. Gayme, C. Meneveau, Filtered actuator disks: theory and application to wind turbine models in large eddy simulation, Wind Energy 22 (10) (2019) 1414–1420.

[27] J.N. Sorensen, W.Z. Shen, Numerical modeling of wind turbine wakes, J. Fluid Eng. 124 (2) (2002) 393–399.

[28] N. Troldborg, J.N. Sorensen, R. Mikkelsen, Numerical simulations of wake characteristics of a wind turbine in uniform inflow, Wind Energy: An International Journal for Progress and Applications in Wind Power Conversion Technology 13 (1) (2010) 86–99.

[29] X. Yang, F. Sotiropoulos, R.J. Conzemius, J.N. Wachtler, M.B. Strong, Large-eddy simulation of turbulent flow past wind turbines/farms: the virtual wind simulator (vwis), Wind Energy 18 (12) (2015) 2025–2045.

[30] W.Z. Shen, J.N. Sørensen, J.H. Zhang, Actuator surface model for wind turbine flow computations, in: Proceedings of European Wind Energy Conference and Exhibition Vol. 7, 2007, pp. 1–10.

[31] I. Dobrev, F. Massouh, M. Rapin, Actuator surface hybrid model, in: J. Phys. Conf., Vol. 75, IOP Publishing, Bristol, UK, 2007, p. 12019.

[32] W. Z. Shen, J. H. Zhang, J. N. Sørensen, The actuator surface model: a new Navier–Stokes based model for rotor computations, J. Sol. Energy Eng. 131 (1).

[33] X. Yang, F. Sotiropoulos, A new class of actuator surface models for wind turbines, Wind Energy 21 (5) (2018) 285–302.

[34] D. Foti, Coherent vorticity dynamics and dissipation in a utility-scale wind turbine wake with uniform inflow, Theor. Appl. Mech. Lett. (2021) 100292.

[35] S. Kang, X. Yang, F. Sotiropoulos, On the onset of wake meandering for an axial flow turbine in a turbulent open channel flow, J. Fluid Mech. 744 (2014) 376–403.

[36] X. Yang, F. Sotiropoulos, On the predictive capabilities of les-actuator disk model in simulating turbulence past wind turbines and farms, in: 2013 American Control Conference, IEEE, 2013, pp. 2878–2883.

[37] Z. Li, X. Yang, Evaluation of actuator disk model relative to actuator surface model for predicting utility-scale wind turbine wakes, Energies 13 (14) (2020) 3574.

[38] Z. Du, M. Selig, A 3-D stall-delay model for horizontal axis wind turbine performance prediction, in: Processing of the 1998 ASME Wind Energy Symposium, 1998, p. 21.

[39] J. Qin, Y. Andreopoulos, X. Jiang, G. Dong, Z. Chen, Efficient coupling of direct forcing immersed boundary-lattice Boltzmann method and finite element method to simulate fluid-structure interactions, Int. J. Numer. Methods Fluid. 92 (6) (2020) 545–572.

[40] X. Yang, X. Zhang, Z. Li, G.-W. He, A smoothing technique for discrete delta functions with application to immersed boundary method in moving boundary simulations, J. Comput. Phys. 228 (20) (2009) 7821–7836.

[41] F. Sotiropoulos, X. Yang, Immersed boundary methods for simulating fluid–structure interaction, Prog. Aero. Sci. 65 (2014) 1–21.

[42] J. Qin, E.M. Kolahdouz, B.E. Griffith, An immersed interface-lattice Boltzmann method for fluid–structure interaction, J. Comput. Phys. 428 (2021) 109807.

[43] J. Smagorinsky, General circulation experiments with the primitive equations: I. the basic experiment, Mon. Weather Rev. 91 (3) (1963) 99–164.

[44] M. Germano, U. Piomelli, P. Moin, W.H. Cabot, A dynamic subgrid-scale eddy viscosity model, Phys. Fluid. Fluid Dynam. 3 (7) (1991) 1760–1765.

[45] L. Ge, F. Sotiropoulos, A numerical method for solving the 3d unsteady incompressible Navier–Stokes equations in curvilinear domains with complex immersed boundaries, J. Comput. Phys. 225 (2) (2007) 1782–1809.

[46] D.A. Knoll, D.E. Keyes, Jacobian-free Newton–krylov methods: a survey of approaches and applications, J. Comput. Phys. 193 (2) (2004) 357–397.

[47] Y. Saad, A flexible inner-outer preconditioned gmres algorithm, SIAM J. Sci. Comput. 14 (2) (1993) 461–469.

[48] M.S. Selig, J.L. Tangler, Development and application of a multipoint inverse design method for horizontal axis wind turbines, Wind Eng. 19 (2) (1995) 91–105.

[49] S. Lee, Inverse design of horizontal axis wind turbine blades using a vortex line method, Wind Energy 18 (2) (2015) 253–266.

[50] J. Hong, M. Toloui, L.P. Chamorro, M. Guala, K. Howard, S. Riley, J. Tucker, F. Sotiropoulos, Natural snowfall reveals large-scale flow structures in the wake of a 2.5-mw wind turbine, Nat. Commun. 5 (2014) 4216.

[51] L.P. Chamorro, S.-J. Lee, D. Olsen, C. Milliren, J. Marr, R. Arndt, F. Sotiropoulos, Turbulence effects on a full-scale 2.5 mw horizontal-axis wind turbine under neutrally stratified conditions, Wind Energy 18 (2) (2015) 339–349.

[52] X. Yang, J. Hong, M. Barone, F. Sotiropoulos, Coherent dynamics in the rotor tip shear layer of utility-scale wind turbines, J. Fluid Mech. 804 (2016) 90–115.

[53] J. Jonkman, S. Butterfield, W. Musial, G. Scott, Definition of a 5-mw Reference Wind Turbine for Offshore System Development, Tech. Rep, National Renewable Energy Lab.(NREL), Golden, CO (United States), 2009.

[54] M.S. Siddiqui, A. Rasheed, M. Tabib, T. Kvamsdal, Numerical investigation of modeling frameworks and geometric approximations on nrel 5 mw wind turbine, Renew. Energy 132 (2019) 1058–1075.

[55] Karhunen, K. Zur Spektraltheorie Stochastischer Prozesse. *Ann. Acad. Sci. Fennicae (1946) AI 34.*

[56] Michel. Loeve. Probability theory: foundations, random sequences, Van Nostrand, New York, NY, 1955.